nature nanotechnology

Article

https://doi.org/10.1038/s41565-023-01520-1

Correlated insulator and Chern insulators in pentalayer rhombohedral-stacked graphene

Received: 20 February 2023

Accepted: 4 September 2023

Published online: 05 October 2023

Check for updates

Tonghang Han[1,6], Zhengguang Lu[1,6], Giovanni Scuri[2,3], Jiho Sung[2,3], Jue Wang[2,3], Tianyi Han[1], Kenji Watanabe[4], Takashi Taniguchi[5], Hongkun Park[2,3] & Long Ju[1]

Rhombohedral-stacked multilayer graphene hosts a pair of flat bands touching at zero energy, which should give rise to correlated electron phenomena that can be tuned further by an electric field. Moreover, when electron correlation breaks the isospin symmetry, the valley-dependent Berry phase at zero energy may give rise to topologically non-trivial states. Here we measure electron transport through hexagonal boron nitride-encapsulated pentalayer graphene down to 100 mK. We observed a correlated insulating state with resistance at the megaohm level or greater at charge density $n = 0$ and displacement field $D = 0$. Tight-binding calculations predict a metallic ground state under these conditions. By increasing D, we observed a Chern insulator state with $C = -5$ and two other states with $C = -3$ at a magnetic field of around 1 T. At high D and n, we observed isospin-polarized quarter- and half-metals. Hence, rhombohedral pentalayer graphene exhibits two different types of Fermi-surface instability, one driven by a pair of flat bands touching at zero energy, and one induced by the Stoner mechanism in a single flat band. Our results establish rhombohedral multilayer graphene as a suitable system for exploring intertwined electron correlation and topology phenomena in natural graphitic materials without the need for moiré superlattice engineering.

Van der Waals heterostructures of two-dimensional (2D) materials have been actively studied to engineer novel device structures and physical properties. In recent years, the introduction of moiré superlattices between adjacent 2D materials has led to a rich spectrum of correlated and topological electron phenomena, including Mott insulators, superconductivity and (quantum) anomalous Hall effects[1–16]. These studies often rely on specific combinations of materials and twist angles—some complex engineering to realize the desired phenomena. It is intriguing to ask if one can achieve electron correlation and topology in crystalline 2D materials without moiré effects. The answer to this question not only clarifies the exact role of the moiré superlattice in already discovered phenomena but can also provide a more general recipe for obtaining similar phenomena in other condensed matter systems where it is hard to introduce a moiré pattern.

Multilayer graphene in the rhombohedral stacking order is potentially such a platform, where a large density of states (DOS) at zero energy (E) derives from a pair of flat conduction and valence bands. Simultaneously, these flat bands carry a large valley-dependent Berry phase due to the pseudospin winding around the Dirac point[17–21]. As a result, both correlated and topological states can emerge from this material without any moiré superlattice. However, previous experiments on devices encapsulated in hexagonal boron nitride (hBN) showed low resistivity (at around the kilohm level) down to millikelvin temperatures at zero displacement field (D) and zero charge density

[1]Department of Physics, Massachusetts Institute of Technology, Cambridge, MA, USA. [2]Department of Chemistry and Chemical Biology, Harvard University, Cambridge, MA, USA. [3]Department of Physics, Harvard University, Cambridge, MA, USA. [4]Research Center for Electronic and Optical Materials, National Institute for Materials Science, Tsukuba, Japan. [5]Research Center for Materials Nanoarchitectonics, National Institute for Materials Science, Tsukuba, Japan. [6]These authors contributed equally: Tonghang Han, Zhengguang Lu. e-mail: longju@mit.edu

https://doi.org/10.1038/s41565-023-01520-1

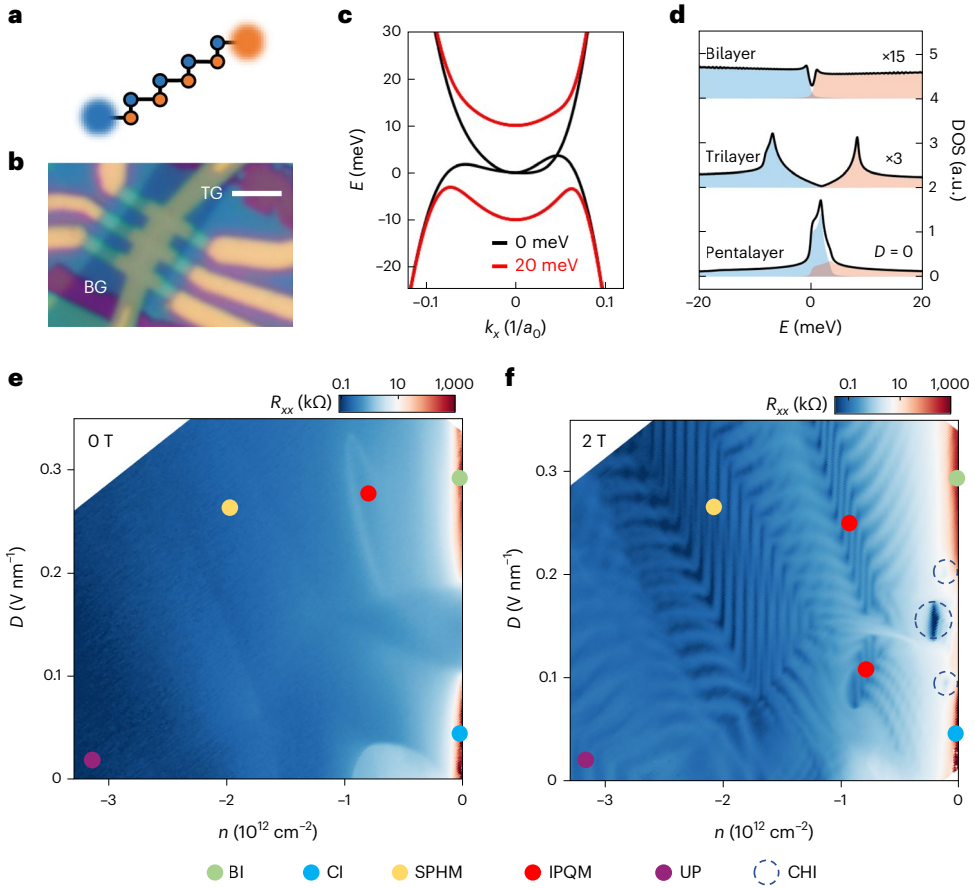

Fig. 1 | Correlation-driven insulator, isospin-symmetry-broken states and Chern insulators in rhombohedral-stacked pentalayer graphene. **a**, Schematic of rhombohedral-stacked pentalayer graphene. The wavefunctions of states in the lowest energy bands concentrate at the sublattices highlighted by the larger dots. **b**, Image of the device where the top gate (TG) and bottom gate (BG) are labelled. Scale bar, 3 µm. **c**, Tight-binding calculations of the energy dispersion of rhombohedral-stacked pentalayer graphene under an interlayer potential $\Delta = 0$ meV (black) and $\Delta = 20$ meV (red) near the K point. With $\Delta = 0$, metallic transport behaviours are expected at charge neutrality. **d**, Tight-binding calculations of DOS in Bernal bilayer, rhombohedral trilayer and pentalayer graphene at $D = 0$, where the bilayer and trilayer data are multiplied by a factor of 15 and 3, respectively, for comparison. The blue and orange shaded areas depict the DOS of the valence and conduction bands, respectively. **e**,**f**, Colour plots of four-probe resistance R_{xx} as a function of the carrier density n and displacement field D measured at an out-of-plane magnetic field of $B = 0$ (**e**) and $B = 2$ T (**f**) at a temperature of 100 mK. Coloured dots label the different phases, which include band insulator (BI), correlated insulator (CI), spin-polarized half metal (SPHM), isospin-polarized quarter metal (IPQM), unpolarized metal (UP) and Chern insulator (CHI) states. The correlated insulator state signifies the strong electron correlation in pristine pentalayer graphene, which is beyond the single-particle picture in **c** and **d**.

(n), which do not necessarily invoke a correlated electron picture[22–24]. Scanning tunnelling spectroscopy studies on rhombohedral-stacked regions of twisted double-bilayer graphene did not show a clean gap either[25,26]. Experiments using suspended graphene devices indeed observed an interacting-induced insulating state, although the measurements and data interpretation suffered from either the two-terminal geometry or the very limited parameter space. Crucially, topological states with clear signatures of quantized longitudinal resistance (R_{xx}) and Hall resistance (R_{xy}) values have not been identified[27–31].

Here we overcame these obstacles using hBN-encapsulated dual-gated pentalayer graphene in the rhombohedral stacking order (Fig. 1a). We purposely avoid the moiré effect by choosing a large twist angle between the graphene and neighbouring hBN layers. As shown in Fig. 1b, the Hall bar device configuration enables accurate measurements of R_{xx} and R_{xy}, and its non-suspended geometry enables access to a wide range of charge density n and displacement field D. At zero D and correspondingly zero interlayer potential difference Δ, our tight-binding calculations predict flat conduction and valence bands near zero energy (Fig. 1c), from which a large DOS emerges (Fig. 1d). This fact points to the possibility of Fermi-surface instability which is different from that driven by the Stoner mechanism in a single band. The latter can also be observed in our device at large D, as we will show in the following. Compared with the number of layers (N) being ≤ 3, the DOS in pentalayer graphene ($N = 5$) is larger due to the $E \propto \pm|k|^N$ energy dispersion of rhombohedral-stacked graphene (Fig. 1d), where k is the electron momentum. In even thicker layers, the screening effect increases with increased N and counteracts the effect of flat bands[31–33]. As a result, $N = 5$ is likely to be close to an ideal thickness for observing electron correlation at zero energy.

Phase diagram of rhombohedral-stacked pentalayer graphene

Figure 1e,f shows the 2D colour plot of the device resistance R_{xx} by tuning n and D at an out-of-plane magnetic field $B = 0$ T and 2 T, respectively. The measurements were taken at a temperature of $T = 100$ mK. Combining both plots, we made the following three observations:

First, an insulating state with R_{xx} as big as 10 MΩ appears at $D = n = 0$. This resistance is three orders of magnitude higher than that in both thinner and thicker hBN-encapsulated rhombohedral-stacked graphene devices[22–24]. This insulator state is clearly beyond the

https://doi.org/10.1038/s41565-023-01520-1

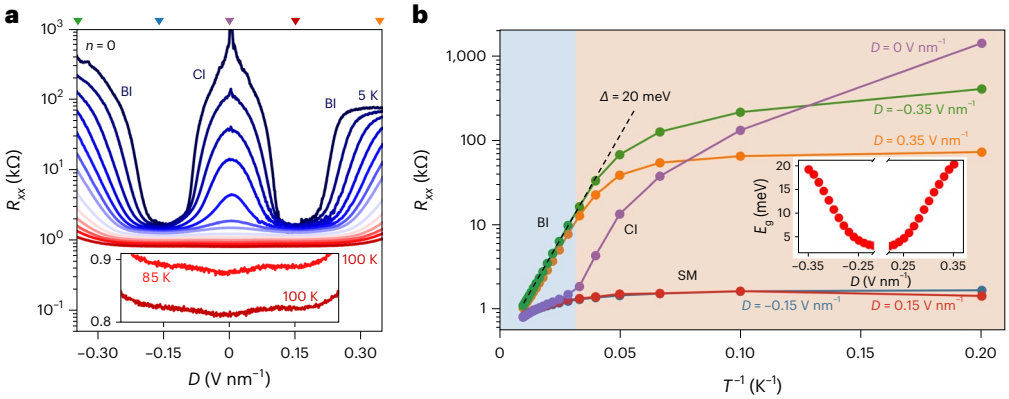

Fig. 2 | Temperature and magnetic field dependence of the correlated insulator state. a, Temperature dependence of the four-probe resistance R_{xx} measured at charge neutrality ($n = 0$) from 5 K to 100 K. Inset: expanded view of R_{xx} versus D at high temperatures of 85 K and 100 K. At high temperatures the resistive state at $D = 0$ disappears and evolves to a dip in R_{xx}, consistent with the large single-particle DOS at $D = 0$. **b**, R_{xx} versus temperature from 5 K to 100 K at five displacement fields corresponding to the coloured triangles in **a** of the same colour. They can be categorized into three groups: correlated insulator (CI), band insulator (BI) and semimetal (SM) states. At high temperatures ($T > 40$ K, blue region) the correlated insulator state resembles the semimetal state, and at low temperatures (orange region), R_{xx} for the correlated insulator state increases dramatically, indicating the gap opening. Inset: bandgap of the band insulator extracted from the thermal activation fitting.

prediction of tight-binding calculations and is a manifestation of gap opening due to electron correlation at zero energy. We will call this a correlated insulator state throughout the manuscript. The insulating state at $D > 0.19$ V nm^{-1} is probably a band insulator, as the interlayer potential Δ will dominate the Hamiltonian at large D.

Second, three states with R_{xx} close to zero emerge in a magnetic field, as indicated by the dashed circles in Fig. 1f. As we will show more data and discuss them in detail later, these states show quantized R_{xy} and we conclude that they are Chern insulators. They are located at finite doping and $D = 0.1$–0.2 V nm^{-1}, neighbouring states with R_{xx} of the order of kilohms at $n = 0$. The Chern insulator states have a strong connection with the correlated insulator state, and they will be the focus of our following discussions.

Third, isospin-polarized metallic states exist at finite D and $n > 0.5 \times 10^{12}$ cm^{-2}. At $B = 0$ T, three regions of the n–D plot can be identified as unpolarized full metal (magenta dot in Fig. 1e), spin-polarized half metal (yellow dot) and isospin-polarized quarter metal (red dot). The degeneracy of these states can be seen from the period of quantum oscillations in Fig. 1f (or more rigorously analysed following so-called Fermiology[23,24]). The spin and valley characters of these states can be deduced from the anomalous Hall resistance (see Extended Data Fig. 4). We note that an elliptical-shaped region in Fig. 1f (shown with the second red dot) also corresponds to the isospin-polarized quarter metal, which is only revealed under a finite magnetic field.

These observations demonstrate a rich collection of electron correlation and topological effects in pentalayer graphene, driven by two distinct mechanisms. The first mechanism originates from the coexistence of flat electron and hole bands near zero energy, resulting in a correlated insulating state. Previous literature has suggested a layer antiferromagnetic (LAF) state as the ground state[19,30]. The second mechanism is the Stoner-type instability that is incurred from a single band with a large DOS, which can be created by opening up the gap of rhombohedral multilayer graphene at large D. The resulting spin-polarized half-metal and isospin-polarized quarter-metal states have also been observed in bilayer and trilayer graphene[23,34–36]. Pentalayer graphene, however, shows both types of correlation effect. We will focus on phenomena due to the first mechanism in the following.

Correlated insulator at zero D and zero n

In Fig. 1d, the single-particle calculation reveals a substantially greater DOS at $D = n = 0$ in pentalayer graphene than in bilayer and trilayer graphene. In the latter systems, low resistances were observed at $D = n = 0$, which aligns with the semimetallic states predicted by the tight-binding calculations[23,24,34–36]. The resistance of pentalayer graphene at $D = n = 0$ is three orders of magnitude higher than that in rhombohedral graphene devices with $N = 2$, 3 and >10 under the same gating conditions (see Extended Data Fig. 3). This is contradictory to the single-particle picture, which predicts a DOS that is >50 times larger in pentalayer graphene than in $N = 2$ or 3. This experimental observation provides direct and strong evidence of electron correlation effects in the zero-energy flat bands of pentalayer rhombohedral graphene.

Next, we explore the correlated insulator state in more detail. Figure 2a shows R_{xx} at $n = 0$ and a range of D in the temperature range of 5–100 K. At high D, R_{xx} decreases when the temperature is increased, as expected for a band insulator state. At zero D, R_{xx} follows the same trend, because the correlated insulator state is thermally excited. At sufficiently high temperatures (see the Fig. 2a inset and Supplementary Fig. 6), the state at zero D becomes even more conducting than that at neighbouring D values. This change indicates the melting of the correlated insulator state into a semimetal with a large DOS as shown in Fig. 1d, and the recovery of the single-particle picture.

The quantitative dependence on temperature, however, is different between the band insulator and correlated insulator states, as revealed in Fig. 2b. At $D = \pm 0.35$ V nm^{-1}, R_{xx} for the band insulator follows an exponential dependence on $1/T$ in the high-temperature region, as indicated by the dashed line, implying the typical thermal activation behaviour of band insulators. The values of the bandgap (E_g) extracted from this fitting are shown in the inset of Fig. 2b, where E_g increases from almost zero at the gap re-opening D to ~20 meV at a higher D value. By contrast, the state at $D = 0$ shows distinct behaviours at low and high temperatures. At low temperatures ($T < 40$ K; orange region), R_{xx} at $D = 0$ is several times higher than that at $D = \pm 0.35$ V nm^{-1}, and up to three orders of magnitude higher than that at $D = \pm 0.15$ V nm^{-1}. The $D = 0$ state clearly indicates insulating behaviour. At high temperatures ($T > 40$ K; blue region), however, the $D = 0$ state shows the same behaviour as the semimetallic state at $D = \pm 0.15$ V nm^{-1}, in contrast to the thermal activation behaviour in the $D = \pm 0.35$ V nm^{-1} gapped state. The transition from insulator-like to semimetal-like behaviour of the state at $D = 0$ clearly differentiates it from the states at $D = \pm 0.35$ V nm^{-1}. We conclude that the insulating behaviour of the $D = 0$ state is due to a gap opened by the electron correlation effect, and at high temperatures this gap disappears so the device shows low resistance, as predicted by the large DOS in the single-particle picture.

https://doi.org/10.1038/s41565-023-01520-1

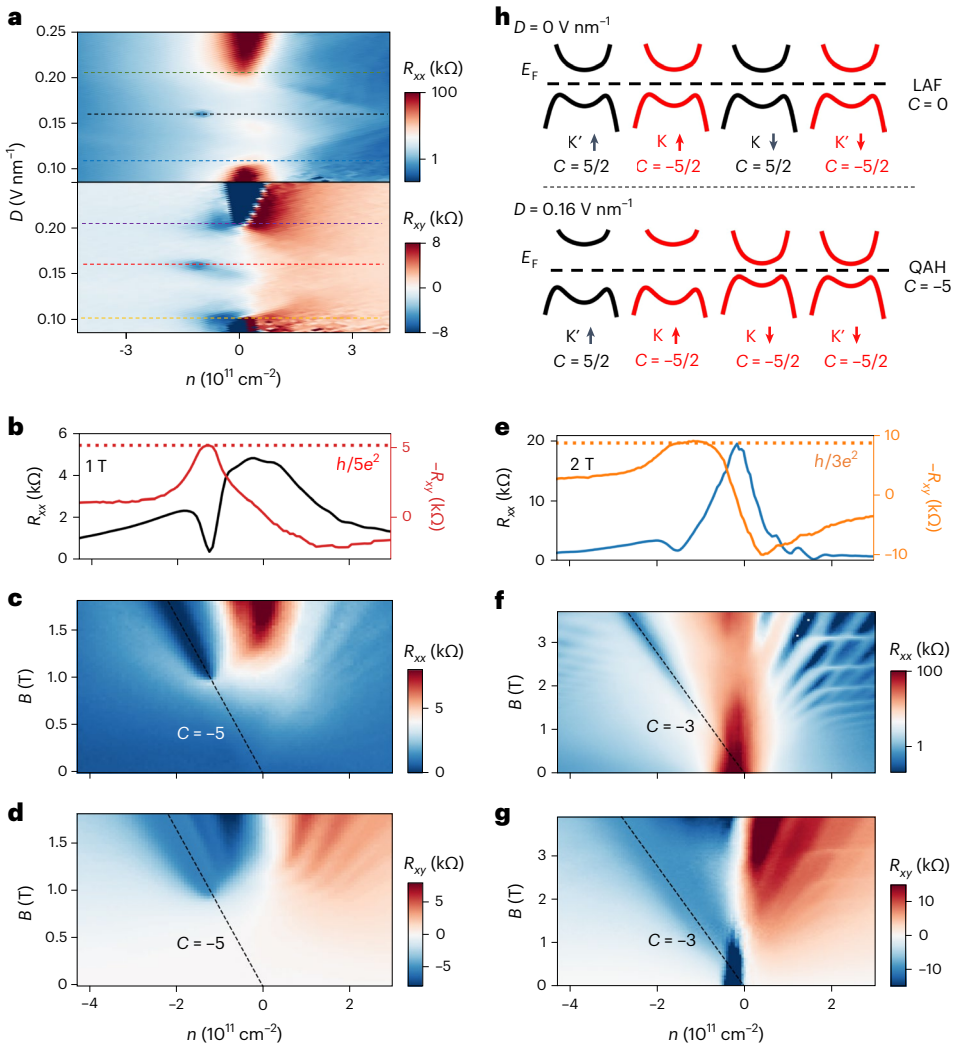

Fig. 3 | Correlation-driven Chern insulator states. a, 2D colour plots for R_{xx} (upper) and R_{xy} (lower) at $B = 1$ T, revealing three Chern insulator states on the hole-doped side in the gap-closing range of D. The state with a Chern number $C = -5$ occurs at $D = 0.16$ V nm^{-1}, and two states with $C = -3$ occur at $D = 0.11$ V nm^{-1} and $D = 0.21$ V nm^{-1}, as indicated by the dashed lines. No signature of a Chern insulator was observed on the electron-doped side. **b**, R_{xx} (black) and R_{xy} (red) corresponding to the dashed lines at $D = 0.16$ V nm^{-1} in **a**. R_{xx} shows a significant dip at the charge density where the R_{xy} is well quantized at $-h/5e^2$, indicating a Chern insulator with $C = -5$. **c**,**d**, 2D colour plots of R_{xx} (**c**) and R_{xy} (**d**) versus n and B at $D = 0.16$ V nm^{-1}. The dashed lines indicate the n–B relation of a $C = -5$ Chern insulator as predicted by Streda's formula. Compared with the faint Landau fan emerging on the electron-doped side, the $C = -5$ state is much more robust and is the only state that appears on the hole-doped side. Below $B = 0.95$ T, the $C = -5$ state terminates sharply, indicating the existence of a competing phase. **e**–**g**, Plots similar to those of **b**–**d**, respectively, which show R_{xx} (blue) and R_{xy} (orange) corresponding to the dashed lines in **a** at $D = 0.11$ V nm^{-1} (**e**) and 2D colour plots of R_{xx} (**f**) and R_{xy} (**g**) versus n and B with $C = -3$. **h**, Schematic of the LAF state at $D = 0$ (upper) and the QAH state at an intermediate D (lower), where the valleys are labelled using K and K′, and the spins are indicated by the arrows. The colour indicates the sign of the Chern number of the valence band of a specific isospin flavour. The net Chern number is 0 at $D = 0$, and it becomes −5 as the bandgap corresponding to one isospin inverts upon applying a displacement field. E_F, Fermi level.

Theories have explored such Fermi-surface instability, and several candidates for a correlated insulating state at $D = n = 0$ have been suggested[37–44], and we examine the possibility of quantum valley Hall (QVH), quantum spin Hall (QSH), quantum anomalous Hall (QAH) and LAF states[19] (see Supplementary Section III). The QVH state, which is layer-polarized, can be ruled out as an explanation of our observation since the device shows symmetric gap-closing and re-opening behaviour with respect to positive and negative D values, as shown in Fig. 2a. The QSH and QAH states can also be ruled out since the two-terminal conductance at $D = n = 0$ is close to zero, indicating the absence of edge states. As a result, the only candidate that is compatible with our observation is the LAF state. Definitive evidence of the LAF state, however, calls for in-depth spectroscopy experiments that can probe the whole band structure at $n = 0$ while D is continuously tuned. This is beyond our current manuscript.

One trivial origin of the insulating state at $D = 0$ is a band insulator with some built-in interlayer potential difference. However, that state should evolve asymmetrically as D is tuned to positive and negative values, and in particular that low-resistance states should not appear on one side of D. By contrast, our data as presented in Fig. 2a show gap-closing behaviour at both positive and negative D values with a mostly symmetric dependence on D. We therefore rule out the built-in potential as the correct explanation of our observation.

Correlation-driven Chern insulator states

We examine the range of $D = 0.1$–0.2 V nm^{-1} in which our device shows a resistance of the order of several kilohms. Figure 3a shows 2D colour plots of R_{xx} and R_{xy} at $B = 1$ T. Large signals appear at around $n = 0$, which are due to the band insulator and correlated insulator states. In addition, three states emerge on the hole-doped side at $D = 0.11$, 0.16 and

https://doi.org/10.1038/s41565-023-01520-1

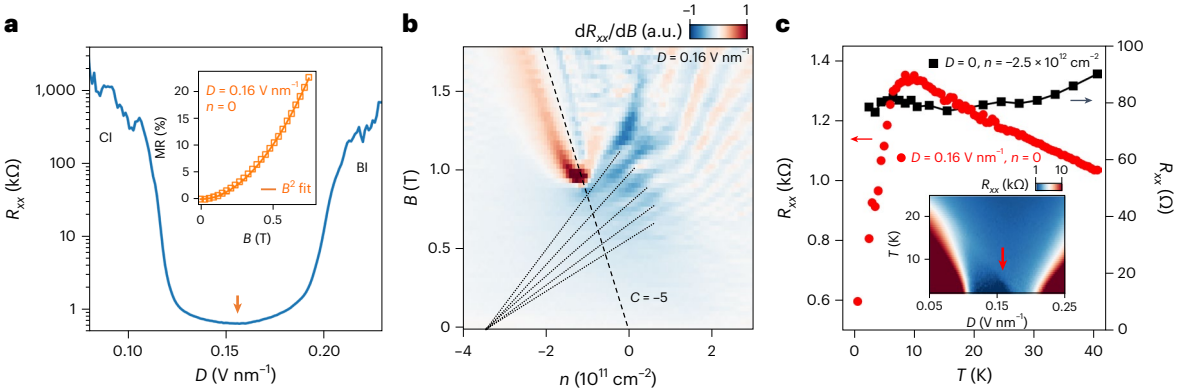

Fig. 4 | The competing phase at $B = 0$. a, R_{xx} versus D at $n = 0$ and $T = 100$ mK. While R_{xx} reaches the megaohm level at small D (correlated insulator) and large D (band insulator), it goes down to well below a kilohm in the intermediate D range. Inset: magnetoresistance (MR) ratio $[R_{xx}(B) - R_{xx}(0)]/R_{xx}(0)$ at $D = 0.16$ V nm^{-1} and $n = 0$ as a function of B. The MR data (orange squares) follow nicely a B^2 dependence, indicating a compensated semimetal phase. **b**, Colour plot of dR_{xx}/dB versus the carrier density n and out-of-plane magnetic field B measured at $D = 0.16$ V nm^{-1} and a temperature of 100 mK. The dashed line indicates the C = −5 state. The dotted lines trace the electron Landau levels, which converge to a negative electron density of 3.4×10^{11} cm^{-2}, agreeing with the semimetal picture. **c**, Temperature-dependent R_{xx} at $D = 0.16$ V nm^{-1} and $n = 0$ (red) and at $D = 0$ and $n = -2.5 \times 10^{12}$ cm^{-2} (black). The red curve increases as T is decreased from high temperature, but it starts to drop quickly with a decrease in T is below 7 K, while the black curve does not show strong temperature dependence at low temperatures. Inset: colour map of R_{xx} as a function of the displacement field D and temperature T measured at $n = 0$. The dark blue region at low temperature hosts the non-monotonic temperature dependence, and the red arrow indicates the $D = 0.16$ V nm^{-1} linecut.

0.21 V nm^{-1}, as indicated by the dashed lines. They start to emerge at 1 T and become fully developed at 2 T, as encircled in Fig. 1f. From the bottom to the top of each of the plots in Fig. 3a, the first state is located at the same D as where the correlated insulator state vanishes, the second state is located where the system is metallic, and the third state is located at the same D as where the band insulator state starts to develop—implying their close relation to the insulator–metal–insulator transitions at $n = 0$ when D is tuned continuously. To investigate these states further, first we show in Fig. 3b the linecuts from Fig. 3a at $D = 0.16$ V nm^{-1}. R_{xy} is quantized at $\frac{h}{5e^2}$, where h is Planck's constant and e is the charge on an electron, and R_{xx} shows a dip at $n = -1.2 \times 10^{11}$ cm^{-2}. These observations indicate a Chern number $C = -5$. Figure 3c,d shows the evolution of R_{xx} and R_{xy} at $D = 0.16$ V nm^{-1} as B is tuned. The dashed lines trace this state, and their slopes agree with $C = -5$ according to the formula of Streda[45]. Similarly, Fig. 3e shows the linecuts of R_{xx} and R_{xy} at $D = 0.11$ V^{-1} and $B = 2$ T, where R_{xy} is quantized at $\frac{h}{3e^2}$ and R_{xx} shows a dip at $n = -1.5 \times 10^{11}$ cm^{-2}. Figure 3f,g shows the evolution of R_{xx} and R_{xy} at $D = 0.11$ V nm^{-1} as B is tuned. Both the quantized value of R_{xy} and the slopes indicate a state with $C = -3$. The state at $D = 0.21$ V nm^{-1} also shows a Chern number $C = -3$, as displayed in Extended Data Fig. 6. For all three states, the plateaus of quantized R_{xy} are significantly broader than those of the states on the electron-doped side.

We understand the $C = -5$ state as a correlation-driven Chern insulator state. The bands at zero energy in pentalayer rhombohedral graphene host a Berry phase of π per spin per valley. As the Berry curvature is concentrated at the band edge when a small gap is opened by the gate electric field, we can integrate it for the lower energy portion of the band and define a valley Chern number. The valley Chern number is 5/2 or −5/2, as shown in Fig. 3h, which evolves with the displacement field and enables direct visualization of the physical picture. We start from the LAF state at zero D. The net Chern number of the system is zero due to the equal number of valence bands with positive and negative C. As D is increased, the applied electrostatic potential will enlarge the gap in two of these isospin copies and shrink the gap in the other two, depending on their layer polarizations (Extended Data Fig. 9). When D is large enough to close and re-open one of the gap-shrunk isospin-polarized bands, the corresponding Chern number will change sign[19,38]. As a result, the net Chern number of the system will be $C = -5$. Such a QAH state at $B = 0$ has been predicted by theory[19,38], but experimental evidence with quantized R_{xx} and R_{xy} has not been observed. In our device, a finite magnetic field of ~0.9 T starts to reveal the $C = -5$ Chern insulator state, which is aligned with the expectation that the QAH state may win the competition with the help of a small magnetic field[38]. The actual ground state in our device at $B = 0$ could be a semimetal, as we will discuss in the next section.

We also attribute Chern insulators as being the origin of the $C = -3$ states, which appear at values of D that are roughly symmetric around the D at which the $C = -5$ state is observed. At the same time, these two values of D define the boundaries between the correlated insulator state, the metallic state and the band insulator state. Both facts imply that the gap of one isospin band structure is closed at these D values (and so is the global gap of the whole device). In these scenarios, counting the total Chern number is more complicated than for the $C = -5$ state, as the subtlety in the band structure and the integration of Berry curvature over occupied states clearly play an important role[20,46,47]. Compared with the $C = -5$ state, which can be explained by the correlation-driven effects applied to the isospin-polarized band structure at zero fillings, a band picture to explain the $C = -3$ states is not clear at this point. We have included more rationale against the integer quantum Hall states as explanations for the $C = -5$ and $C = -3$ states in 'Rationale to rule out the integer quantum Hall state as an explanation for the $C = -5$ state' in the Methods.

Similar Chern insulators were observed at the negative D side (Extended Data Fig. 8). Considering the large twist angles between graphene and any hBN flakes, the moiré potential is negligible for both the top and bottom graphene/hBN interfaces. Therefore, the phase diagrams of the positive and negative D values are symmetric. Our observations invite further theoretical and experimental efforts for a complete understanding of the details.

Competing semimetallic phase at zero B field

The $C = -5$ state vanishes at $B = 0.9$ T, with an abrupt change of R_{xx} and R_{xy}. This indicates the existence of a competing phase with the $C = -5$ QAH state instead of a disorder- or temperature-limited observation of the latter. Figure 4a shows R_{xx} in the phase-transition range of D at $n = B = 0$ and $T = 100$ mK. Residing between the correlated insulator and band insulator states, which both reach around the megaohm level, the competing phase shows a resistance of ~600 Ω. Furthermore, the magnetoresistance at $n = 0$ follows a quadratic dependence on B, as shown in the inset, which is typical for a compensated semimetal.

These observations indicate that the competing phase is a semimetal, which is consistent with the single-particle band structure of pentalayer graphene as shown in Fig. 1c. Furthermore, we analyse in Fig. 4b the derivative of R_{xx} versus B, which reveals a Landau fan of electron states converging to a negative electron density of 3.4×10^{11} cm^{-2}. This fact agrees with the compensated semimetal picture[48]. We note that the hotspot at $B = 0.9$ T and $n = -1.1 \times 10^{11}$ cm^{-2} corresponds to the abrupt phase transition from the $C = -5$ Chern insulator to the semimetal, while the Landau levels on the electron-doped side disappear gradually.

The temperature-dependent R_{xx} of this competing phase, however, is quite unusual. As shown in Fig. 4c, R_{xx} increases as the temperature is decreased in the range of $T = 7$–40 K. This is consistent with the semimetal picture in which the density of thermally excited carriers is reduced as the temperature is decreased. At $T < 7$ K, R_{xx} decreases quickly as the temperature is decreased. One may think this trend in the low-temperature range can be explained by reduced phonon-scattering as the temperature is decreased. However, our data for the large-n metallic state rule out this explanation, as shown in Fig. 4c and Extended Data Fig. 10. This non-monotonic temperature dependence exists for a range of D, shown as the blue triangular region in the inset of Fig. 4c. The origin of this behaviour is not clear, although the trend is intriguing: will R_{xx} keep decreasing (even eventually to zero) as we lower the temperature further? Our observation invites further measurements at lower and well-calibrated electronic temperatures. The answer to this question could possibly shed light on the competing phase, and reveal other correlated and topological states such as superconductivity and QAH[19,49].

Conclusions

Our results demonstrate a collection of correlated and topological phases in a single material. These phenomena in a natural 2D crystal provide a pathway for exploring exotic quantum phenomena without involving moiré superlattices. Recent theories have suggested rhombohedral multilayer graphene as a topologically non-trivial chiral $p + ip$ superconductor with chiral Majorana edge modes[50] as well as a valley-polarized Wigner crystal[51]. Our work establishes rhombohedral multilayer graphene as a highly tunable platform for the study of strongly correlated and topological states. The very different behaviour of pentalayer graphene from thinner and much thicker graphene flakes also points to the layer thickness as an important means of tuning in further experiments on rhombohedral graphene.

Online content

Any methods, additional references, Nature Portfolio reporting summaries, source data, extended data, supplementary information, acknowledgements, peer review information; details of author contributions and competing interests; and statements of data and code availability are available at https://doi.org/10.1038/s41565-023-01520-1.

References

1. Cao, Y. et al. Correlated insulator behaviour at half-filling in magic-angle graphene superlattices. *Nature* **556**, 80–84 (2018).
2. Cao, Y. et al. Unconventional superconductivity in magic-angle graphene superlattices. *Nature* **556**, 43–50 (2018).
3. Sharpe, A. L. et al. Emergent ferromagnetism near three-quarters filling in twisted bilayer graphene. *Science* **365**, 605–608 (2019).
4. Serlin, M. et al. Intrinsic quantized anomalous Hall effect in a moiré heterostructure. *Science* **367**, 900–903 (2020).
5. Chen, G. et al. Evidence of a gate-tunable Mott insulator in a trilayer graphene moiré superlattice. *Nat. Phys.* **15**, 237–241 (2019).
6. Chen, G. et al. Signatures of tunable superconductivity in a trilayer graphene moiré superlattice. *Nature* **572**, 215–219 (2019).
7. Chen, G. et al. Tunable correlated Chern insulator and ferromagnetism in a moiré superlattice. *Nature* **579**, 56–61 (2020).
8. Regan, E. C. et al. Mott and generalized Wigner crystal states in WSe_2/WS_2 moiré superlattices. *Nature* **579**, 359–363 (2020).
9. Tang, Y. et al. Simulation of Hubbard model physics in WSe_2/WS_2 moiré superlattices. *Nature* **579**, 353–358 (2020).
10. Wang, L. et al. Correlated electronic phases in twisted bilayer transition metal dichalcogenides. *Nat. Mater.* **19**, 861–866 (2020).
11. Yankowitz, M. et al. Tuning superconductivity in twisted bilayer graphene. *Science* **363**, 1059–1064 (2019).
12. Cao, Y. et al. Tunable correlated states and spin-polarized phases in twisted bilayer–bilayer graphene. *Nature* **583**, 215–220 (2020).
13. Shen, C. et al. Correlated states in twisted double bilayer graphene. *Nat. Phys.* **16**, 520–525 (2020).
14. Liu, X. et al. Tunable spin-polarized correlated states in twisted double bilayer graphene. *Nature* **583**, 221–225 (2020).
15. Polshyn, H. et al. Electrical switching of magnetic order in an orbital Chern insulator. *Nature* **588**, 66–70 (2020).
16. Chen, G. et al. Tunable orbital ferromagnetism at noninteger filling of a moiré superlattice. *Nano Lett.* **22**, 238–245 (2022).
17. Min, H. & MacDonald, A. H. Electronic structure of multilayer graphene. *Prog. Theor. Phys. Suppl.* **176**, 227–252 (2008).
18. Zhang, F., Sahu, B., Min, H. & MacDonald, A. H. Band structure of ABC-stacked graphene trilayers. *Phys. Rev. B* **82**, 035409 (2010).
19. Zhang, F., Jung, J., Fiete, G. A., Niu, Q. & MacDonald, A. H. Spontaneous quantum Hall states in chirally stacked few-layer graphene systems. *Phys. Rev. Lett.* **106**, 156801 (2011).
20. Koshino, M. & McCann, E. Trigonal warping and Berry's phase N_π in ABC-stacked multilayer graphene. *Phys. Rev. B* **80**, 165409 (2009).
21. Yang, N., Li, C., Tang, Y. & Yelgel, C. Electronic structure of ABC-stacked multilayer graphene and trigonal warping: a first principles calculation. *J. Phys. Conf. Ser.* **707**, 012022 (2016).
22. Shi, Y. et al. Electronic phase separation in multilayer rhombohedral graphite. *Nature* **584**, 210–214 (2020).
23. Zhou, H. et al. Half- and quarter-metals in rhombohedral trilayer graphene. *Nature* **598**, 429–433 (2021).
24. Zhou, H., Xie, T., Taniguchi, T., Watanabe, K. & Young, A. F. Superconductivity in rhombohedral trilayer graphene. *Nature* **598**, 434–438 (2021).
25. Pierucci, D. et al. Evidence for flat bands near the Fermi level in epitaxial rhombohedral multilayer graphene. *ACS Nano* **9**, 5432–5439 (2015).
26. Kerelsky, A. et al. Moiréless correlations in ABCA graphene. *Proc. Natl Acad. Sci. USA* **118**, e2017366118 (2021).
27. Weitz, R. T., Allen, M. T., Feldman, B. E., Martin, J. & Yacoby, A. Broken-symmetry states in doubly gated suspended bilayer graphene. *Science* **330**, 812–816 (2010).
28. Freitag, F., Trbovic, J., Weiss, M. & Schönenberger, C. Spontaneously gapped ground state in suspended bilayer graphene. *Phys. Rev. Lett.* **108**, 76602 (2012).
29. Bao, W. et al. Stacking-dependent band gap and quantum transport in trilayer graphene. *Nat. Phys.* **7**, 948–952 (2011).
30. Velasco, J. et al. Transport spectroscopy of symmetry-broken insulating states in bilayer graphene. *Nat. Nanotechnol.* **7**, 156–160 (2012).
31. Myhro, K. et al. Large tunable intrinsic gap in rhombohedral-stacked tetralayer graphene at half filling. *2D Mater.* **5**, 045013 (2018).
32. Pamuk, B., Baima, J., Mauri, F. & Calandra, M. Magnetic gap opening in rhombohedral-stacked multilayer graphene from first principles. *Phys. Rev. B* **95**, 075422 (2017).
33. Jia, J., Gorbar, E. V. & Gusynin, V. P. Gap generation in ABC-stacked multilayer graphene: screening versus band flattening. *Phys. Rev. B* **88**, 205428 (2013).

34. Zhou, H. et al. Isospin magnetism and spin-polarized superconductivity in Bernal bilayer graphene. *Science* **375**, 774–778 (2022).
35. de la Barrera, S. C. et al. Cascade of isospin phase transitions in Bernal-stacked bilayer graphene at zero magnetic field. *Nat. Phys.* **18**, 771–775 (2022).
36. Seiler, A. M. et al. Quantum cascade of correlated phases in trigonally warped bilayer graphene. *Nature* **608**, 298–302 (2022).
37. Zhang, F., Min, H., Polini, M. & MacDonald, A. H. Spontaneous inversion symmetry breaking in graphene bilayers. *Phys. Rev. B* **81**, 041402 (2010).
38. Jung, J., Zhang, F. & MacDonald, A. H. Lattice theory of pseudospin ferromagnetism in bilayer graphene: competing interaction-induced quantum Hall states. *Phys. Rev. B* **83**, 115408 (2011).
39. Nandkishore, R. & Levitov, L. Quantum anomalous Hall state in bilayer graphene. *Phys. Rev. B* **82**, 115124 (2010).
40. Vafek, O. & Yang, K. Many-body instability of Coulomb interacting bilayer graphene: renormalization group approach. *Phys. Rev. B* **81**, 041401 (2010).
41. Lemonik, Y., Aleiner, I. & Fal'Ko, V. I. Competing nematic, antiferromagnetic, and spin-flux orders in the ground state of bilayer graphene. *Phys. Rev. B* **85**, 245451 (2012).
42. Kharitonov, M. Antiferromagnetic state in bilayer graphene. *Phys. Rev. B* **86**, 195435 (2012).
43. Xu, D. H. et al. Stacking order, interaction, and weak surface magnetism in layered graphene sheets. *Phys. Rev. B* **86**, 201404 (2012).
44. Sun, K., Yao, H., Fradkin, E. & Kivelson, S. A. Topological insulators and nematic phases from spontaneous symmetry breaking in 2D Fermi systems with a quadratic band crossing. *Phys. Rev. Lett.* **103**, 046811 (2009).
45. Streda, P. Theory of quantised Hall conductivity in two dimensions. *J. Phys. C* **15**, L717 (1982).
46. Li, J., Tupikov, Y., Watanabe, K., Taniguchi, T. & Zhu, J. Effective Landau level diagram of bilayer graphene. *Phys. Rev. Lett.* **120**, 47701 (2018).
47. McCann, E. & Fal'ko, V. I. Landau-level degeneracy and quantum Hall effect in a graphite bilayer. *Phys. Rev. Lett.* **96**, 86805 (2006).
48. Slizovskiy, S., McCann, E., Koshino, M. & Fal'ko, V. I. Films of rhombohedral graphite as two-dimensional topological semimetals. *Commun. Phys.* **2**, 164 (2019).
49. Kopnin, N. B., Ijäs, M., Harju, A. & Heikkilä, T. T. High-temperature surface superconductivity in rhombohedral graphite. *Phys. Rev. B* **87**, 140503 (2013).
50. Ghazaryan, A., Holder, T., Berg, E. & Serbyn, M. Multilayer graphenes as a platform for interaction-driven physics and topological superconductivity. *Phys. Rev. B* **107**, 104502 (2023).
51. Calvera, V., Kivelson, S. A. & Berg, E. Pseudo-spin order of Wigner crystals in multi-valley electron gases. *Low Temp. Phys.* **49**, 679–700 (2023).

Methods

Identification of rhombohedral pentalayer graphene and sample fabrication

The pentalayer graphene and hBN flakes were prepared by mechanical exfoliation onto SiO_2/Si substrates. As shown in Extended Data Fig. 1, the rhombohedral domains of pentalayer graphene were identified using near-field infrared microscopy[52], confirmed using Raman spectroscopy and isolated by cutting using an atomic force microscope (Bruker)[53]. The van der Waals heterostructure was made following a dry-transfer procedure. We picked up the top hBN and pentalayer graphene using polypropylene carbonate film and landed it on a prepared bottom stack comprising an hBN and graphite bottom gate. We intentionally misaligned the straight edges of the flakes to avoid the formation of a moiré superlattice. The device was then etched into a Hall bar structure using standard electron-beam lithography and reactive-ion etching. We then deposited a NiCr alloy top layer to form a dual-gate device.

Transport measurements

The device was measured in a dilution refrigerator (LD250, Bluefors) with an electronic temperature around 100 mK. Lock-in amplifiers (SR830, Stanford Research Systems) were used to measure the longitudinal and Hall resistance R_{xx} and R_{xy}, respectively, with an AC voltage bias of 200 μV at a frequency at 17.77 Hz.

Tight-binding calculations

The single-particle band structure of the rhombohedral N-layer graphene is calculated using the $2N$-band continuum model. The Hamiltonian and the parameters are taken from previous literature[18].

Extended Data Figure 2 shows the calculated band structure and DOS of rhombohedral multilayer graphene (N = 2, 3, 4, 5, 7 and 9) at zero interlayer potential (Δ = 0). Owing to remote hoppings, the band structure deviates from $E \approx k^N$ at low energy. For bilayer and trilayer graphene, the DOS at zero energy is small due to the approximate $E \approx k^N$ dispersion. For rhombohedral graphene of around five layers, there is a large DOS at zero energy, which leads to Fermi-surface instability and the correlated insulator state. For graphene thicker than five layers, the band overlap and screening effect become larger, which weakens the interaction effect. This may explain the absence of the correlated insulator at $D = n = 0$ for thick rhombohedral graphene[22]. As a result, rhombohedral pentalayer graphene probably has the optimal number of layers, where the low-energy bands are the flattest and the interaction is the strongest among all the N-layer samples.

Correlated insulator in pentalayer graphene

We show the calculated and experimental results from bilayer and trilayer graphene to support the conclusion of a correlated insulator state in pentalayer graphene. In Extended Data Fig. 3a we present the DOS from the tight-binding calculations at $D = 0$ for N = 2, 3 and 5. In Extended Data Fig. 3b–d we present the resistance as a function of n and D for our devices with N = 2, 3 and 5. At $D = n = 0$, both the N = 2 and 3 devices show small a DOS and a resistance of around a few kilohms, which is typical for metallic states in graphene. By contrast, the DOS at $D = n = 0$ for N = 5 is more than 50 times bigger than its N = 2 and 3 counterparts. In a single-particle picture, such a large DOS should result in a much smaller resistance in N = 5 compared with its N = 2 and 3 counterparts. However, the experimentally measured value of R_{xx} at >10 MΩ is around four orders of magnitude larger than that seen for N = 2 and 3. This obvious contradiction to the single-particle picture clearly points to electron correlation effects, as we concluded.

Phase diagram for both electron and hole doping

Extended Data Figure 4a,b shows the colour plots of four-probe resistance R_{xx} as a function of the carrier density n and displacement field D for the hole-doping side and the electron-doping side measured at $B = 0$ and a temperature of 100 mK. At large D, the phase diagram looks similar to that of the previous study in bilayer and trilayer graphene. At intermediate and small D, the semimetal and correlated insulator states emerge and dominate the neighbouring regions.

The degeneracy of the isospin-polarized metal is inferred from the degeneracy of the Landau levels, as described in the main text. However, the exact nature of the half metal requires further measurement. Extended Data Figure 4c,e shows the Hall resistance R_{xy} as a function of the out-of-plane magnetic field at the red and yellow dots of panel **a**. The quarter metal (panel **c**) shows a clear anomalous Hall effect and magnetic hysteresis, indicating a net valley polarization. By contrast, the half metal (panel **e**) does not show an anomalous Hall effect or magnetic hysteresis, indicating the absence of net valley polarization. Therefore, we conclude the half metal to be spin-polarized and valley-unpolarized.

Temperature dependence of the correlated insulator

We include a more complete set of temperature-dependent data for the correlated insulator. Extended Data Figure 5a shows a complete dataset of the temperature-dependent R_{xx} in the range between 2 K and 40 K. The correlated insulator develops below 30 K. The two white arrows indicate the semimetal phase with an anomalous temperature dependence in the low-temperature region, corresponding to Fig. 4c. Extended Data Figure 5b shows the temperature dependence of R_{xx} between 40 K and 100 K. The $D = 0$ state is shown as a bump in R_{xx} at 40 K, which becomes flatter as the temperature is increased. Eventually it becomes a dip at high temperatures. This evolution corresponds to the melting of the correlated insulator state into a metal with a large DOS and the recovery of the single-particle picture.

The $C = -3$ Chern insulator state

Data for the $C = -3$ state at $D = 0.21$ V nm^{-1} are presented in Extended Data Fig. 6, which demonstrate similar behaviour to the $C = -3$ state at $D = 0.11$ V nm^{-1} as shown in Fig. 3. Similar to Fig. 4b in the main text, we show a derivative plot of the $C = -3$ state at $D = 0.11$ V nm^{-1} in Extended Data Fig. 7. On the basis of dR_{xx}/dB in panel **a** and dR_{xy}/dn in panel **b**, we found that the $C = -3$ state is the only state at the hole side under low magnetic fields and it traces all the way to zero magnetic field. The integer quantum Hall states on the electron side disappear at a higher magnetic field. The $C = -5$ state has a competing semimetal phase at $B = 0$, which dominates the state at just below 0.9 T. By contrast, there is no such a competing phase for the $C = -3$ state, so the $C = -3$ state traces all the way down to $B = 0$.

Rationale to rule out the integer quantum Hall state as an explanation for the $C = -5$ state

Now we explain why the $C = -5$ state cannot be an integer quantum Hall state. For rhombohedral-stacked graphene with N layers, when considering only nearest-neighbour hopping, the integer quantum Hall states near zero energy should first appear at $C = \pm 2N$. This is due to the N almost-degenerate Landau levels at zero energy and the four-fold degeneracy of spin and valley[17]. In our device, however, the $C = \pm 10$ states are completely missing. It is likely that the pseudospin degeneracy has already been lifted at $D = 0.16$ V nm^{-1}, and the observed $C = -5$ state corresponds to one of the four pseudospin copies of the band structure. However, if we apply a simple integer quantum Hall picture to one pseudospin-polarized band structure, one would expect a $C = 5$ state on the electron-doped side to appear at an even smaller B field, due to the more dispersive conduction band and a larger quantum Hall gap correspondingly (see Fig. 1c). In addition, integer quantum Hall states corresponding to C = −6, −7, −8 and so on should appear at even lower B since those gaps are bigger than that of the $C = -5$ state[17,20]. The experimental data, however, are contradictory to these expectations: the $C = 5, -6, -7, -8$ and other quantum Hall states are completely missing in Fig. 3a when the $C = -5$ state has fully developed with a quantized R_{xy} value. This is distinct from the case of bilayer graphene, where the $C = \pm 2$ and ± 4 states appear at a similar B value[27,54].

Even if we include more hopping terms in the tight-binding model, the integer quantum Hall picture still cannot explain our data. In this case, the trigonal warping effect distorts the $E \propto \pm|k|^N$ energy dispersion and creates a three-fold rotational symmetric valence band (see Supplementary Fig. 1)[18,20]. At close to zero energy, the integer quantum Hall states correspond to $C = -3m$, where the 3 is due to the three hole pockets and the integer m is the number of isospin flavours at the Fermi level. Previous experiments on bilayer and trilayer graphene all show data consistent with this picture[23,29,36,55]. The $C = -5$ state observed in our device, however, clearly deviates from this integer quantum Hall picture. At hole densities larger than 2.8×10^{12} cm^{-2}, the Fermi surface recovers to a single circle and the quantum Hall sequence no longer follows $C = -3m$ (see Supplementary Fig. 1). However, this density threshold is one order of magnitude larger than 1×10^{11} cm^{-2}, the density at which we start to observe the $C = -5$ state[22,28,35].

We also emphasize that the $C = -3$ states are probably Chern insulators for the following reasons. (1) There are no other states with finite Chern numbers on the hole-doped side. (2) The plateau of R_{xy} for the $C = -3$ state is much wider than that of the states on the electron-doped side. (3) These states persist to a lower magnetic field than any other integer quantum Hall states at the same displacement field (see Fig. 3e and the Extended Data figures).

Data availability

The data shown in the main figures are available from the Harvard Dataverse Repository at https://doi.org/10.7910/DVN/ISWXLA. The datasets generated during and/or analysed during this study are available from the corresponding author upon reasonable request.

References

52. Ju, L. et al. Topological valley transport at bilayer graphene domain walls. *Nature* **520**, 650–655 (2015).
53. Li, H. et al. Electrode-free anodic oxidation nanolithography of low-dimensional materials. *Nano Lett.* **18**, 8011–8015 (2018).
54. Geisenhof, F. R. et al. Quantum anomalous Hall octet driven by orbital magnetism in bilayer graphene. *Nature* **598**, 53–58 (2021).
55. Varlet, A. et al. Anomalous sequence of quantum Hall liquids revealing a tunable Lifshitz transition in bilayer graphene. *Phys. Rev. Lett.* **113**, 116602 (2014).

Acknowledgements

We acknowledge helpful discussions with F. Zhang, T. Senthil, L. Levitov, L. Fu, Z. Dong and A. Patri. L.J. acknowledges support from a Sloan Fellowship. Work by Tonghang Han was supported by NSF grant number DMR- 2225925. The device fabrication of this work was supported by the STC Center for Integrated Quantum Materials, NSF grant number DMR-1231319. Device fabrication was carried out at the Harvard Center for Nanoscale Systems and MIT.Nano. Part of the device fabrication was supported by the USD(R&E) under contract no. FA8702-15-D-0001. K.W. and T.T. acknowledge support from the JSPS KAKENHI (grant numbers 20H00354, 21H05233 and 23H02052) and World Premier International Research Center Initiative (WPI), MEXT, Japan. H.P. acknowledges support by NSF grant number PHY-1506284 and AFOSR grant number FA9550-21-1-0216. A portion of this work was performed at the National High Magnetic Field Laboratory, which is supported by the National Science Foundation Cooperative Agreement No. DMR-2128556* and the State of Florida.

Author contributions

L.J. supervised the project. Tonghang Han, Z.L., G.S., J.S. and J.W. performed the DC magneto-transport measurements. Tonghang Han and Tianyi Han fabricated the devices. K.W. and T.T. grew the hBN single crystals. H.P. contributed to the data analysis. All authors discussed the results and wrote the paper.

Competing interests

The authors declare no competing interests.

Additional information

Extended data is available for this paper at https://doi.org/10.1038/s41565-023-01520-1.

Supplementary information The online version contains supplementary material available at https://doi.org/10.1038/s41565-023-01520-1.

Correspondence and requests for materials should be addressed to Long Ju.

Peer review information *Nature Nanotechnology* thanks Yuan Cao and the other, anonymous, reviewers for their contribution to the peer review of this work.

https://doi.org/10.1038/s41565-023-01520-1

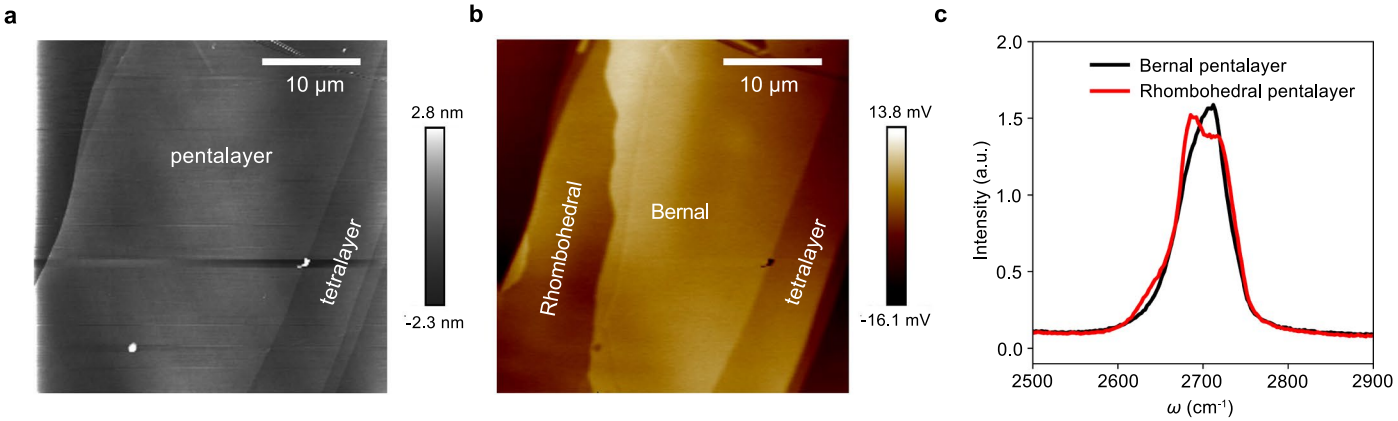

Extended Data Fig. 1 | Identification of rhombohedral pentalayer graphene. **a**, AFM topography map of a pentalayer graphene sample on a SiO_2/Si substrate. (The small region on the right corresponds to a graphene tetralayer.) **b**, Near-field infrared nanoscopy image of the same pentalayer graphene sample as in **a**, showing different contrast on the pentalayer region. The bright region corresponds to Bernal stacking and the darker region corresponds to rhombohedral stacking. **c**, Raman spectra taken at rhombohedral and Bernal stacking domains in the pentalayer graphene sample as in **b**. ω is the Raman shift.

https://doi.org/10.1038/s41565-023-01520-1

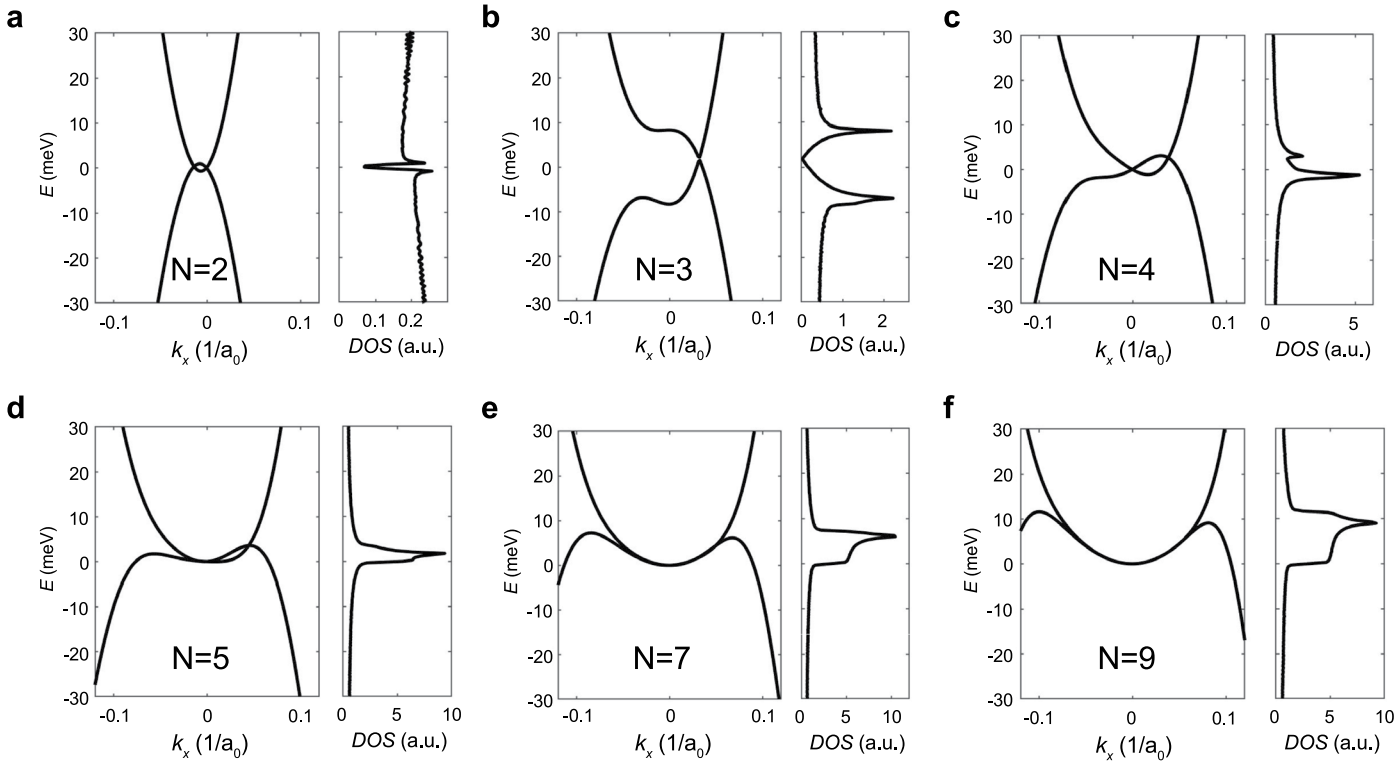

Extended Data Fig. 2 | Single particle band structure and density of states of rhombohedral multilayer graphene. a–f, Tight-binding calculation of single-particle band structure and density of states (DOS) for rhombohedral multilayer graphene (layer number $N = 2, 3, 4, 5, 7, 9$). Due to the remote hopping terms, the band structure deviates from $E \approx k^N$ at low energy. The rhombohedral pentalayer graphene has the flattest band among all layer numbers.

https://doi.org/10.1038/s41565-023-01520-1

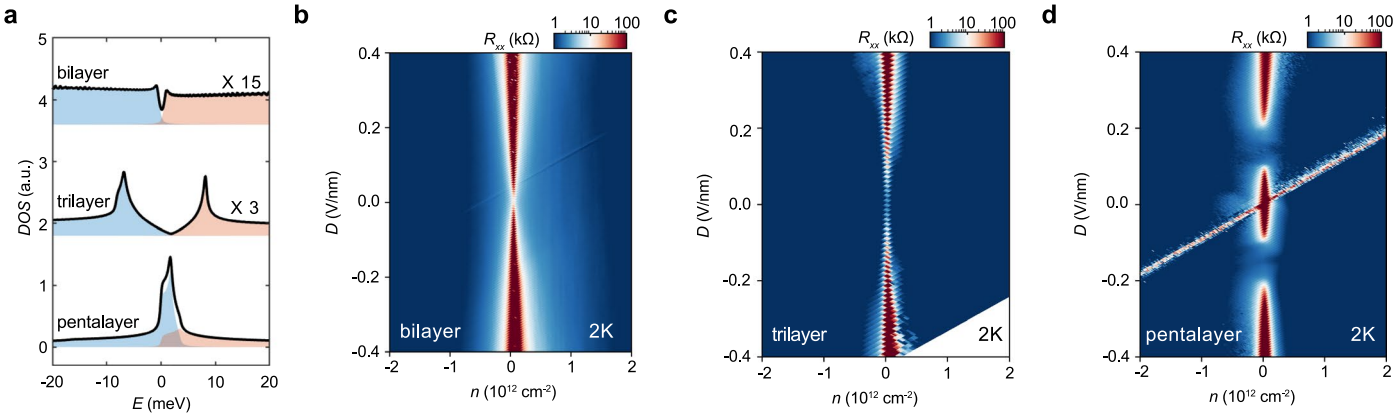

Extended Data Fig. 3 | Correlated insulator at $n = D = 0$ in pentalayer rhombohedral graphene. a, The calculated single-particle density of states (DOS) in Bernal bilayer, rhombohedral trilayer (time a factor of 15 and 3 for comparison), and pentalayer graphene at $D = 0$. The blue and orange shaded areas depict the DOS of the valence and conduction band. **b**–**d**, The n-D R_{xx} map of the bilayer, trilayer and pentalayer graphene measured at 2 K. Pentalayer graphene has a much larger DOS and band overlap at $n = 0$ compared to the bilayer and trilayer case and expects to be more conducting at $D = n = 0$. However, both bilayer and trilayer graphene are conducting at $D = n = 0$, while an insulating state appears at $D = n = 0$ in pentalayer graphene, indicating the non-single-particle origin of the insulating state. The off-diagonal line in the n-D map of pentalayer graphene is due to the big contact resistance when the bottom gate is zero.

https://doi.org/10.1038/s41565-023-01520-1

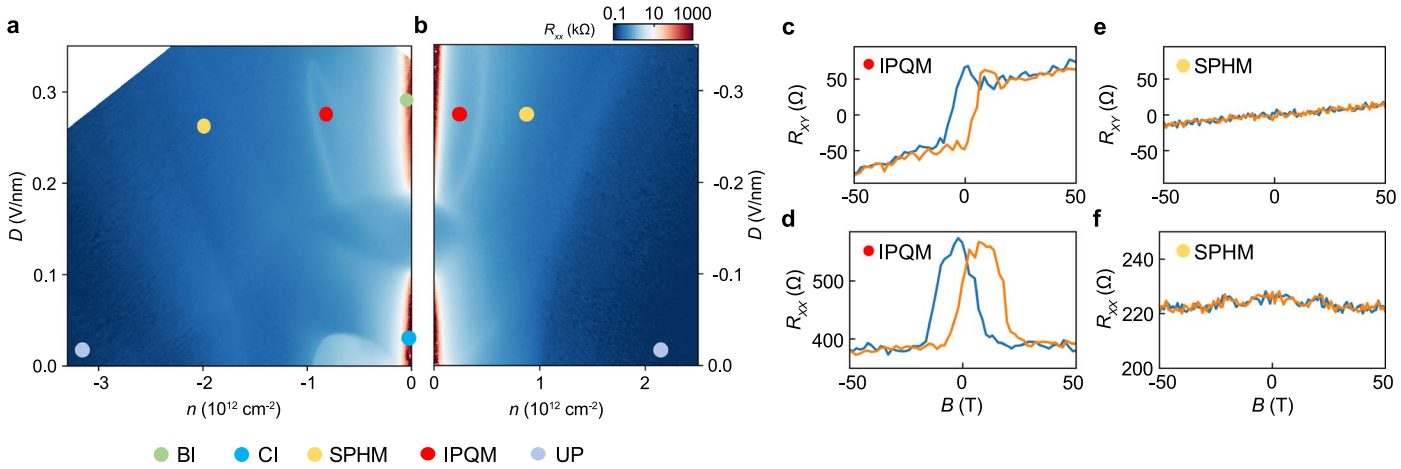

Extended Data Fig. 4 | Phase diagram for both electron and hole doping. **a, b**, Color plots of four-probe resistance R_{xx} as a function of carrier density n and displacement field D for the hole doping side and electron doping side measured at $B = 0$ and a temperature of 100 mK. Colored dots label different phases including band insulator (BI), correlated insulator (CI), spin-polarized half metal (SPHM), isospin-polarized quarter metal (IPQM) and unpolarized metal (UP). **c, d**, Hall resistance R_{xy} and longitudinal resistance R_{xx} as a function of the out-of-plane magnetic field at the red dot in **a**. **e, f**, R_{xy} and R_{xx} at the yellow dot in **a**. The quarter metal **c** & **d** shows a clear anomalous Hall effect and magnetic hysteresis, indicating a net valley polarization. While the half metal **e** & **f** does not show anomalous Hall effect or magnetic hysteresis, indicating the absence of net valley polarization. Therefore, we conclude the half metal to be spin polarized but valley unpolarized.

https://doi.org/10.1038/s41565-023-01520-1

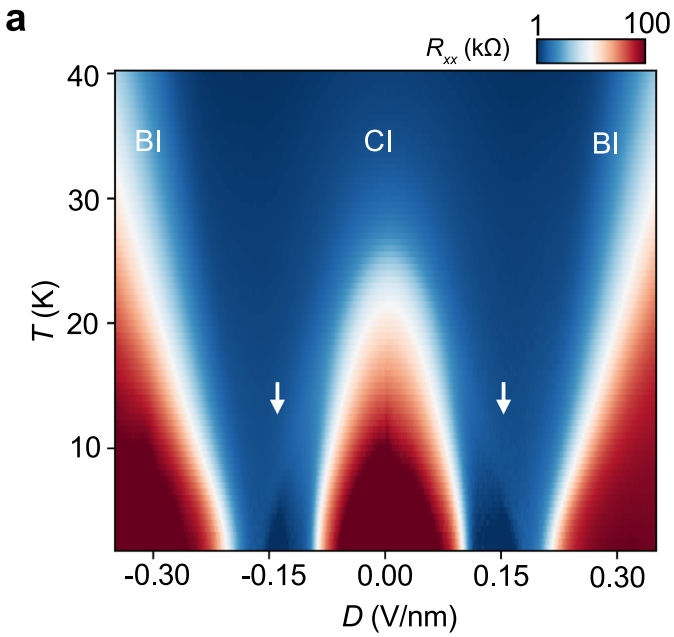

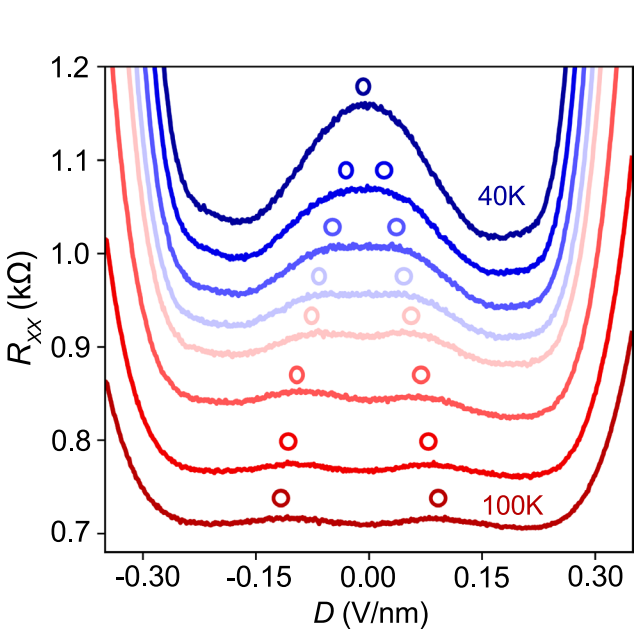

Extended Data Fig. 5 | Additional temperature dependence data of the correlated insulator. a, Temperature dependence of the four-probe resistance R_{xx} measured at charge neutrality ($n = 0$). BI and CI stand for band insulator and correlated insulator. The correlated insulator develops below ~ 30 K. The two white arrows indicate the semimetal phase with an anomalous temperature dependence at the low-temperature region, discussed in Fig. 4c. **b**, R_{xx} versus D at even higher temperatures. As the temperature is increased, the resistive state at $D = 0$ disappears and evolves to a dip in R_{xx}. Circles trace the center of the bumps in R_{xx}.

https://doi.org/10.1038/s41565-023-01520-1

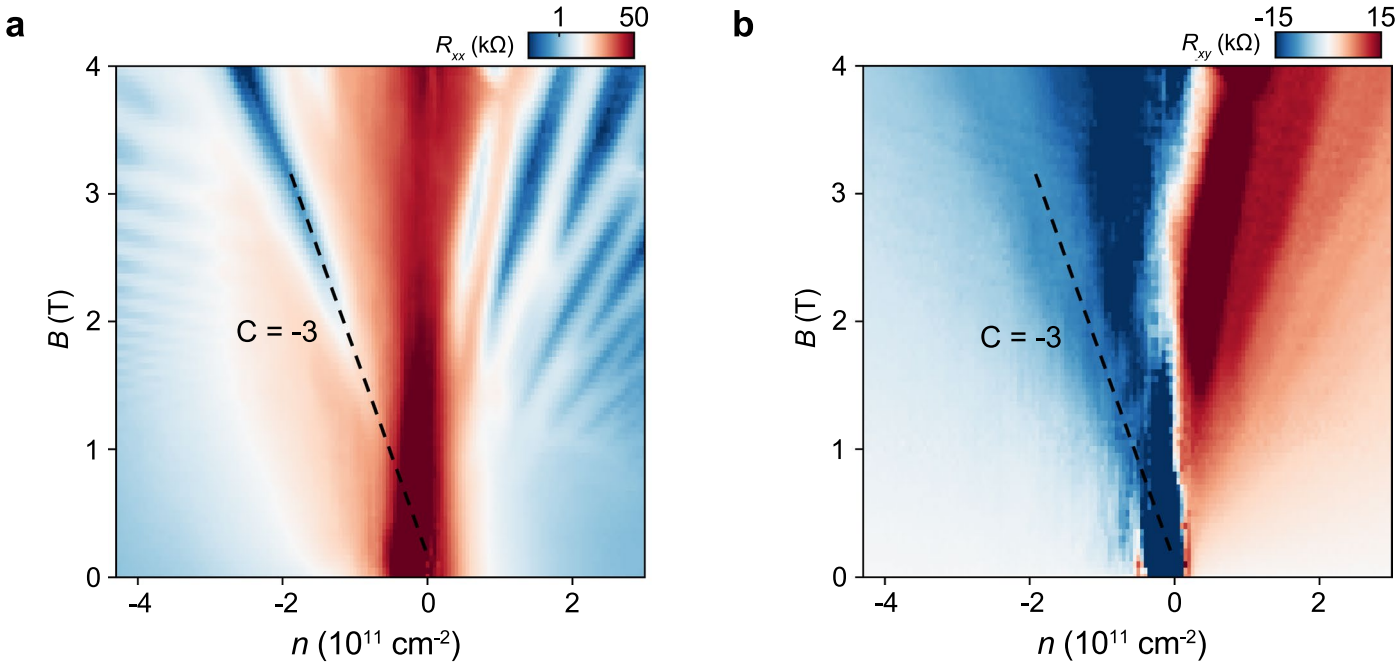

Extended Data Fig. 6 | The C = -3 state at D = 0.21 V/nm. a, b, 2D color plot of R_{xx} and R_{xy} versus carrier density n and out-of-plane magnetic field B taken at D = 0.21 V/nm at a temperature of 100 mK. The dashed line indicates the C = -3 state. The C = -3 state is the only visible state on the hole doping side at low magnetic fields, in contrast to the electron side where all Landau levels appear at a similar magnetic field.

https://doi.org/10.1038/s41565-023-01520-1

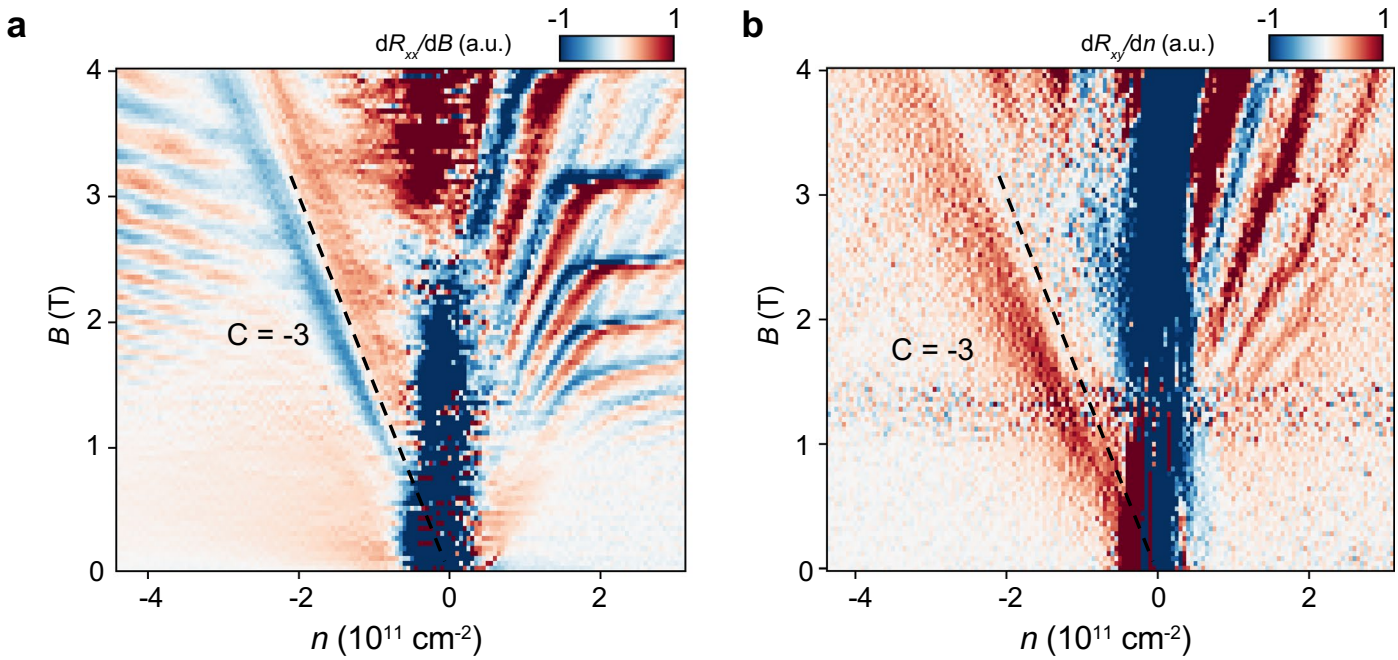

Extended Data Fig. 7 | Tracing the *C* = -3 state towards zero magnetic field. **a**, 2D color plot of dR_{xx}/dB versus carrier density *n* and out-of-plane magnetic field *B* taken at *D* = 0.11 V/nm at a temperature of 100 mK. The dashed line indicates the *C* = -3 state. **b**, 2D color plot of dR_{xy}/dn versus carrier density *n* and out-of-plane magnetic field *B* taken at *D* = 0.11 V/nm at a temperature of 100 mK. The dashed line indicates the *C* = -3 state. The *C* = -3 state is the only visible state on the hole doping side at low magnetic field and traces all the way to 0 T. On the electron side, a complete set of Landau levels is observed and disappears at around 1.5 T.

https://doi.org/10.1038/s41565-023-01520-1

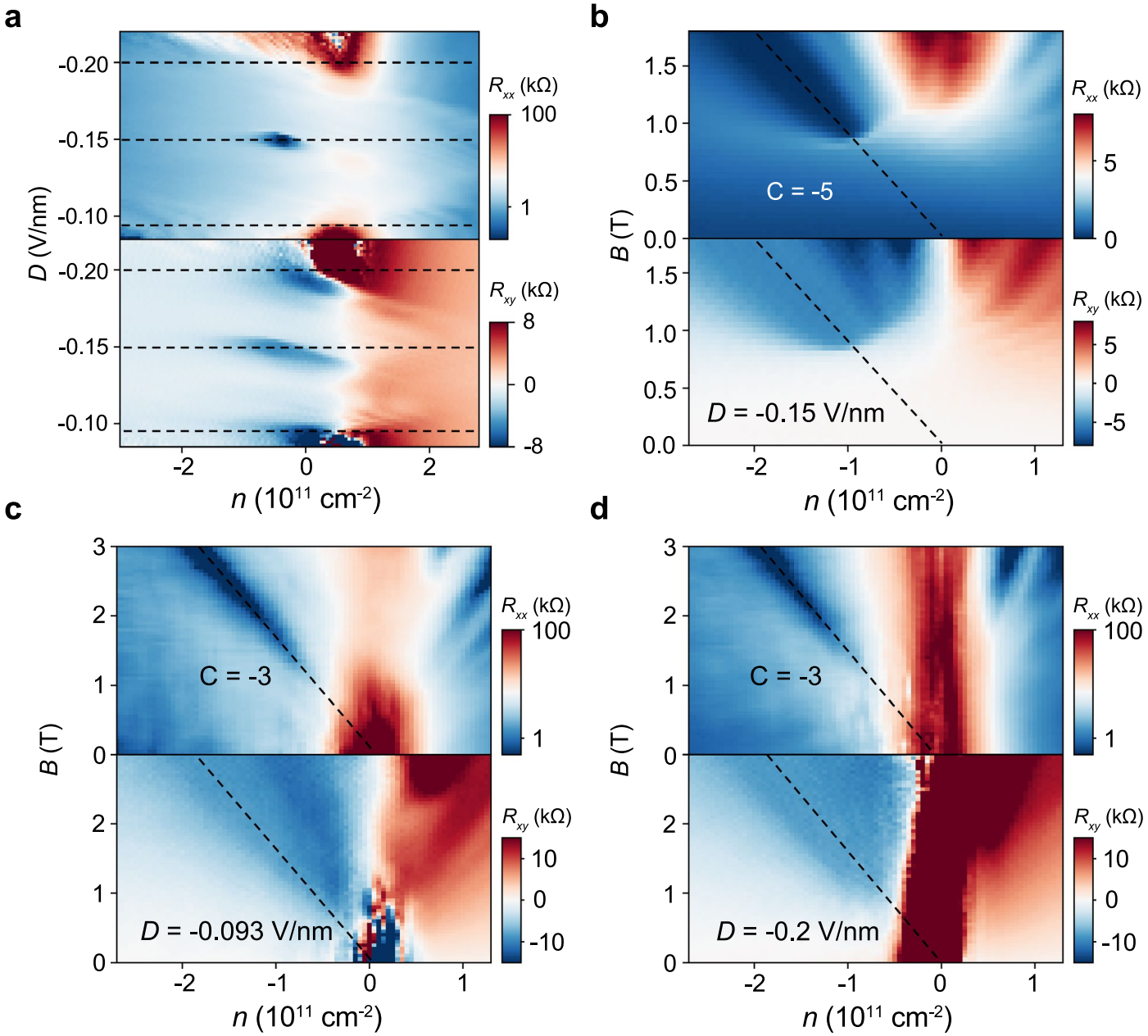

Extended Data Fig. 8 | Chern insulators at the negative side of *D*. **a**, 2D color plots of *Rxx* (upper panel) and *Rxy* (lower panel) at $B = 1$ T, revealing three Chern insulator states at the hole-doped side in the gap-closing range of *D*. The state with a Chern number $C = -5$ happens at $D = -0.15$ V/nm, while two states with $C = -3$ happen at $D = -0.093$ V/nm and $D = -0.2$ V/nm, as indicated by the dashed lines. **b**, **c**, **d**, 2D color plots of *Rxx* (upper panel) and *Rxy* (lower panel) versus *n* and *B* at $D = -0.15$ V/nm, -0.093 V/nm and -0.2 V/nm respectively. The dashed lines indicate the *n*-*B* relation of the Chern insulators as predicted by the Streda formula. These results are consistent with those of the positive *D* side.

https://doi.org/10.1038/s41565-023-01520-1

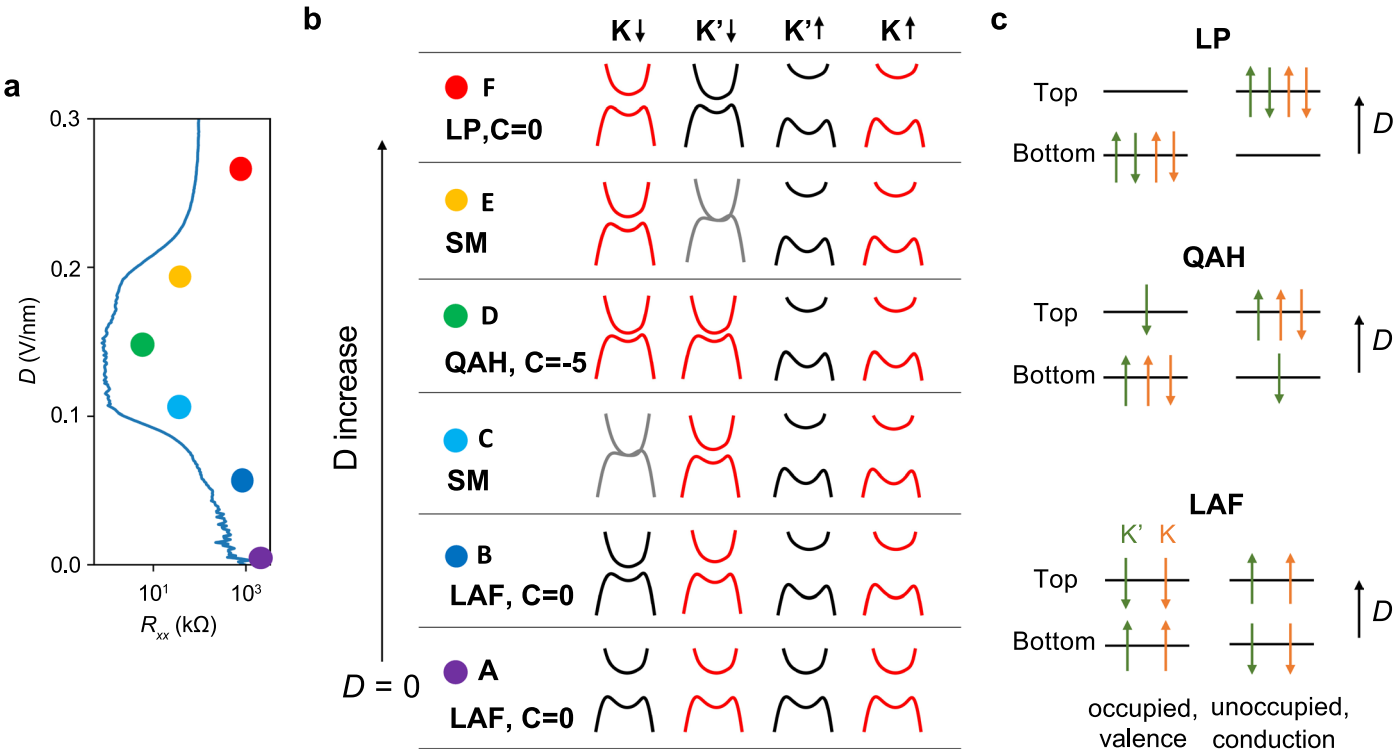

Extended Data Fig. 9 | Evolution of the band structure at charge-neutrality with *D*. **a**, R_{xx} measured at $n = 0$ at 2 K. **b**, The band structure schematic of each isospin flavor at charge-neutrality under different D values. The colored dots correspond to the states in **a**, including LAF (layer antiferromagnet), SM (semimetal), QAH (quantum anomalous Hall) and LP (layer polarized state). The color of each band represents the valley Chern number (black: 5/2, red: -5/2), while the band with a grey color indicates the gap-closing case. **c**, The layer polarization of the LP, QAH and LAF state. The layer polarization of both conduction and valence band for each isospin flavor is shown, where green and orange color corresponds to the K' and K valley. At $D = 0$, the system starts with the LAF state where charges are evenly distributed in the top and bottom layer in a spin-polarized manner (point A). As D increases, the gap of spin up (down) flavor expands (shrinks) due to its layer configuration (point B). It is important to note that the gap sizes of the two valleys with the same spin may differ. Consequently, one of the two gaps closes and reopens first (point C), leading to a situation where the gap of the K valley inverts while the gap of the K' valley remains the same, resulting in the so-called QAH state (point D). Moreover, the layer polarization becomes partially polarized at this stage. If D continues to increase, the gap of the other valley eventually closes and reopens (point E), leading to the fully layer-polarized state (point F).

https://doi.org/10.1038/s41565-023-01520-1

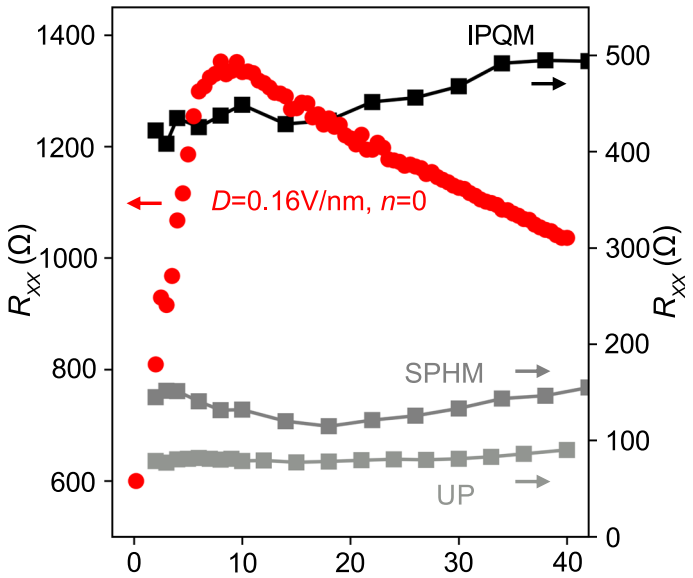

Extended Data Fig. 10 | Temperature dependence of the SPHM, IPQM and UP states. Temperature-dependent R_{xx} at $D = 0.16$ V/nm and $n = 0$ (red), $D = 0$ and $n = -2.5*10^{12}cm^{-2}$ (light grey, UP), $D = 0.26$ V/nm and $n = -1.9*10^{12}cm^{-2}$ (dark grey, SPHM), and $D = 0.26$ V/nm and $n = -0.8*10^{12}cm^{-2}$ (black, IPQM).